TWENTY FIRST EUROPEAN ROTORCRAFT FORUM

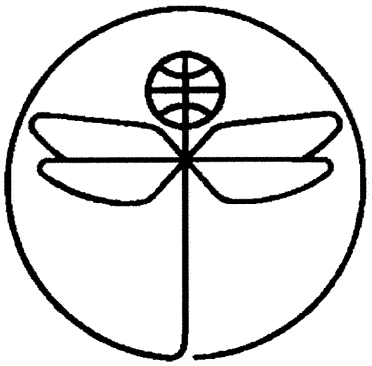

Paper No II.9

FLOW FIELD ANALYSIS OF A MODEL PROP ROTOR IN HOVER

BY

Gloria K. Yamauchi
NASA Ames Research Center

and

Wayne Johnson
Johnson Aeronautics

USA

August 30 - September 1, 1995

SAINT - PETERSBURG, RUSSIA

FLOW FIELD ANALYSIS OF A MODEL PROP ROTOR IN HOVER

Gloria K. Yamauchi
NASA Ames Research Center
Moffett Field, CA, U.S.A.

and

Wayne Johnson
Johnson Aeronautics
Palo Alto, CA, U.S.A.

ABSTRACT

The flow field of a highly-twisted model prop rotor was analyzed using a thin-layer Navier-Stokes analysis. Modifications to the blade root and far-field boundary conditions in the analysis were investigated. Limitations of the single-block grid generator were encountered near the blade root when modeling the blade. The collective pitch in the analysis was adjusted to match the measured thrust. Calculations were then compared with measured hover performance, surface pressures, and wake geometry. Differences in calculated and measured figure of merit ranged from less than one per cent at low thrust to 7 per cent at high thrust. Comparisons of section normal force coefficient improved with increasing radial station. For both low and high thrust levels, surface pressure calculations improved with increasing radial station. Tip vortex descent rate and contraction rate were initially less than the measured rates.

NOMENCLATURE

a_∞	freestream sound speed	p_∞	free stream static pressure
c	chord	r	blade radial coordinate
c_{ref}	reference chord, chord at 0.75 radial station	R	blade radius
C_n	section normal force/$(0.5\rho_\infty(\Omega r)^2 c)$	Re	Reynolds number, $\Omega R c_{ref}/\nu_\infty$
C_p	$(p-p_\infty)/(0.5\rho_\infty(\Omega r)^2)$	x,y,z	inertial coordinates
C_q	section torque/$(0.5\rho_\infty(\Omega R)^2 R c_{ref})$	u,v,w	nondimensional inertial space velocities
C_t	section thrust/$(0.5\rho_\infty(\Omega R)^2 c_{ref})$	z	axial distance from rotor plane
C_T	thrust/$(\pi R^2\rho_\infty(\Omega R)^2)$	ν_∞	kinematic viscosity at sea level
C_Q	torque/$(\pi R^3\rho_\infty(\Omega R)^2)$	ρ_∞	freestream density
FM	figure of merit, $\frac{C_T^{1.5}}{\sqrt{2}C_Q}$	Ω	rotor speed
j,k,ℓ	grid indices	ξ,η,ζ	blade-fixed computational coordinates
M_{tip}	blade tip Mach number, $\Omega R/a_\infty$		

1. Introduction

The tilt rotor is poised to play a significant role in the future of civil aviation. However, there is still much to be learned about tilt rotor behavior, both aerodynamically and acoustically. In particular, the stall behavior of tilt rotor blades is believed to be very different from conventional helicopter blades in hover. For the same mean blade lift, the tilt rotor blade provides better performance than a helicopter blade. The difference in hover performance between the two rotors can be directly attributed to the differences in rotor blade geometry. Physically, the tilt rotor blade has a smaller aspect ratio (approximately 60% of a helicopter blade), taper from root to tip (helicopter blades usually only have taper near the tip), thicker airfoils (on the order of 30% thick at the root), and a nonlinear twist distribution with extremely high twist at the blade root (in contrast, a conventional helicopter blade is linearly twisted over the majority of the blade span). The physical differences are required since the tilt rotor blade not only experiences flow regimes such as hover and helicopter (or edgewise) flight, but also axial flight. Therefore, the blade must include characteristics of a helicopter blade and propeller blade. The difficult question to answer is how these characteristics combine to influence the blade fluid dynamic environment which then provides a noticeable improvement in hover performance compared to the helicopter rotor.

There is insufficient experimental data for tilt rotors available to help answer this question . References 1-3 present hover performance data for isolated tilt rotors. Reference 4 presents wake shadowgraphs from a model prop rotor in hover. Using the same model prop rotor, Ref. 5 presents blade surface pressure and hover performance measurements. There are no visualization measurements in the literature, however, which reveal the flow behavior on the blade surface. These measurements are crucial in determining if calculations are accurately predicting the onset and growth of stalled regions, which in turn affect performance.

Predicting aerodynamic performance for stalled or near-stalled conditions is very difficult; many analyses use empirical corrections under these conditions. Currently, computational analyses originally developed for helicopter rotors are being used to model tilt rotor geometries. The geometry and flow conditions of tilt rotor blades can easily test the limitations of these analyses. The ultimate objective of the designer is to predict performance without the need for empiricism. Fundamental studies examining the behavior of the blade flow field at incipient stall conditions aid in achieving this objective. A reliable viscous analysis is required for this type of investigation. Conventional helicopter blade geometries have been studied using viscous analyses, but there are few investigations of tilt rotor blades (see Refs. 6-8, for example).

The objective of this work is to assess the ability of a state-of-the-art, thin-layer, Navier-Stokes analysis to predict general flow features of a highly-twisted prop rotor in hover. The analysis is based on the work of Ref. 9, which has shown promising correlation results for helicopter rotor blade airloads (Refs. 9-11). The model prop rotor (Refs. 4-5) is selected for this correlation study since surface pressures, performance, and wake geometry measurements exist. Also, the prop rotor has a twist distribution similar to a tilt rotor. Exercising the analysis for the prop rotor geometry provides the groundwork to pursue a more comprehensive investigation of modern full-scale, tilt rotor geometries.

This study first discusses the analysis, including modifications to the boundary conditions. The computational grid is described next, followed by descriptions of the model prop rotor experiments. Comparisons of calculations with measurements are then presented; specific findings from the investigation are summarized and recommendations for future work are given.

2. Description of Analysis

The analysis solves the thin-layer Navier-Stokes equations cast in a general nonorthogonal coordinate system (Ref. 12),

$$\partial_\tau \hat{\mathbf{Q}} + \partial_\xi \hat{\mathbf{E}} + \partial_\eta \hat{\mathbf{F}} + \partial_\zeta \hat{\mathbf{G}} = \frac{1}{\mathrm{Re}} \partial_\zeta \hat{\mathbf{S}} \qquad (1)$$

where

$$\mathbf{Q} = [\,\rho \;\; \rho u \;\; \rho v \;\; \rho w \;\; e\,]^{\mathbf{T}} \;, \quad \hat{\mathbf{Q}} = \mathbf{Q}/J \qquad (2)$$

$\hat{\mathbf{E}}$, $\hat{\mathbf{F}}$, $\hat{\mathbf{G}}$ are the convective flux vectors and $\hat{\mathbf{S}}$ is the viscous flux vector using the thin-layer approximation. The flux vectors have been normalized by the Jacobian J. u,v, and w represent the velocity components in the Cartesian inertial frame. The density, mass fluxes, and energy per unit volume are nondimensionalized by the far-field reference quantities. Re is the Reynolds number based on M_{tip} and a reference chord (defined as the chord at 0.75R for this investigation). The reference chord and sound speed are the characteristic length and velocity scales, respectively. The equation of state for a perfect gas and Eq. 1 describe the entire flow field. The blade-fixed computational coordinates (Fig. 1) are defined by (ξ,η,ζ); the curvilinear coordinate system is fixed relative to the blade surface.

3. Numerical Solution

The solution procedure used in this investigation has evolved from numerical schemes and techniques originally used to solve fixed-wing problems. Modifications to a fixed-wing analysis were made by Srinivasan during a series of studies investigating tip-vortex formation on fixed-wings with different tips (see Ref. 13). The analysis was further modified to calculate rotor flows in hover and forward flight (Ref. 14-15); rotor wake effects, however, were computed by a separate analysis. In 1990, Ref. 9 incorporated major modifications to the analysis which included upwinding for all three (instead of just one) coordinate directions. The upwinding scheme was adapted from the work of Ref. 16. Source terms, to calculate the flow in the blade-fixed coordinate system, and wake capturing features were also included which eliminated the need for an external wake calculation. As described in Ref. 9, the right-hand side of Eq. 1 (after discretization) employs the upwind-biased, flux-difference splitting scheme; a Lower-Upper-Symmetric Gauss-Seidel (LU-SGS) scheme is used for the implicit operator. A monotone upstream-centered scheme for conservative laws (MUSCL) is used to achieve 2nd- or 3rd-order accuracy with flux limiters. The space metrics are evaluated using a finite volume formulation, while a finite difference formulation is used for the time metrics. The turbulence model used is the Baldwin-Lomax model. This modified version of the flow

solver was named the Transonic Unsteady Rotor Navier-Stokes (TURNS) code. TURNS is the analysis used as a starting point for the present investigation.

4. Boundary Conditions

At the blade surface, a no-slip condition is used with a finite velocity due to blade rotation. The surface pressure is obtained through the normal momentum equation and the density is evaluated by the adiabatic wall condition. Since the hover condition is assumed to be steady and symmetric for this study, a periodic flow condition is used in the azimuthal direction; therefore, only one blade is modeled.

In Ref. 9, the inertial velocity components at the blade root plane were obtained by assuming a zero velocity gradient in the spanwise direction. In this investigation, the root plane boundary was modified to be more representative of a rotor blade and center body (Ref. 17). The center body is assumed to rotate with the blade, similar to a tilt rotor blade and spinner. The root plane is now treated with a no-slip condition, similar to the blade surface. Reference 12 states that if a vertical and horizontal wall are being analyzed with the thin-layer equations, the walls should be treated as a single surface, otherwise, the neglected viscous terms in the spanwise direction (for the vertical wall) should be added. This approach was used in Ref. 18 in the analysis of the viscous flow over a wing-fuselage combination. However, the neglected terms in the η-(spanwise) direction were not included in the present study for several reasons. First, the objective was to simulate a no-flow-through surface at the root and not to capture viscous behavior at the blade-root juncture. Second, even if the extra terms were added, the grid spacing in the spanwise direction must be greatly refined near the root in order to capture any boundary layer formation. This is not possible with the current grid generator and the large blade root twist being studied. Therefore, the modification made is considered a justified compromise between the original boundary condition implementation at the root and the procedure used by Ref. 18.

To prevent flow recirculation in the computational domain, the far-field flow is determined by superimposing the flow from a three-dimensional sink (placed at the center of rotation) and momentum theory (Ref. 19). The sink strength calculation of Ref. 19 was modified for this investigation (Ref. 17). The strength is now calculated based on the mass flux leaving the lower boundary, rather than the calculated rotor thrust. The changes described above to the root and far-field boundary conditions improved tilt rotor performance results (Ref. 17).

5. Computational Grid

The computational grid used in this study is a three-dimensional C-H grid composed of stacked two-dimensional C-grids. The C-grids conform to the blade surface; aft of the blade trailing edge at each spanwise station, the grid collapses to a slit. At the blade tip, the grid again collapses to a slit, resulting in a beveled tip. The outer grid is adjusted and smoothed to accommodate the periodic boundary condition which requires the front and back of the outer grid to match. The baseline grid size is 181x53x53, defined as 181 points in the wrap-around (or ξ-) direction, 53 points in the spanwise (or η-) direction, and 53 points in the normal (or ζ-) direction (Fig. 1). Of the 181 points in the wrap-around direction, 145 define the blade profile; 36 of the 53 grid stations in the spanwise direction define the blade from root to tip. The outer boundaries are one rotor diameter above and below the rotor plane. The distance to the first point off the blade surface in the normal direction is 0.00004 c_{ref} (chord at 0.75R). The spanwise location of the outer boundary is one rotor radius beyond the blade tip.

Constructing a computational grid for the prop rotor blade surface was more difficult than anticipated. The blade is more like a propeller blade than a tilt rotor blade in terms of profile. The airfoil sections have rounded, rather than sharp, trailing edges. The rounded trailing edges introduced problems in gridding, which will be discussed later. To insure accurate airfoil section geometries, airfoil coordinates were measured on one blade at ten radial stations. These coordinates were used to calculate the blade section twist and chord length. Figure 2 shows the chord and twist distributions obtained from the measurements. The curves in Figs. 2a) and b) were subsequently represented by polynomials for a smooth distribution. The coordinates, twist, and chord length for each section were then incorporated into a grid generator code. The resulting grid was wavy in the spanwise direction and although appearing smooth in the chordwise direction, resulting trial calculations of surface pressures clearly indicated smoothing of the coordinates was also required in the chordwise direction. Therefore, the coordinates of each airfoil section were run through a program (Ref. 20) which smoothed the curvature of the profiles. This significantly improved the surface smoothness in the chordwise direction. To improve the smoothness in the spanwise direction, an additional ten profiles were generated by interpolating between measured (and smoothed) profiles.

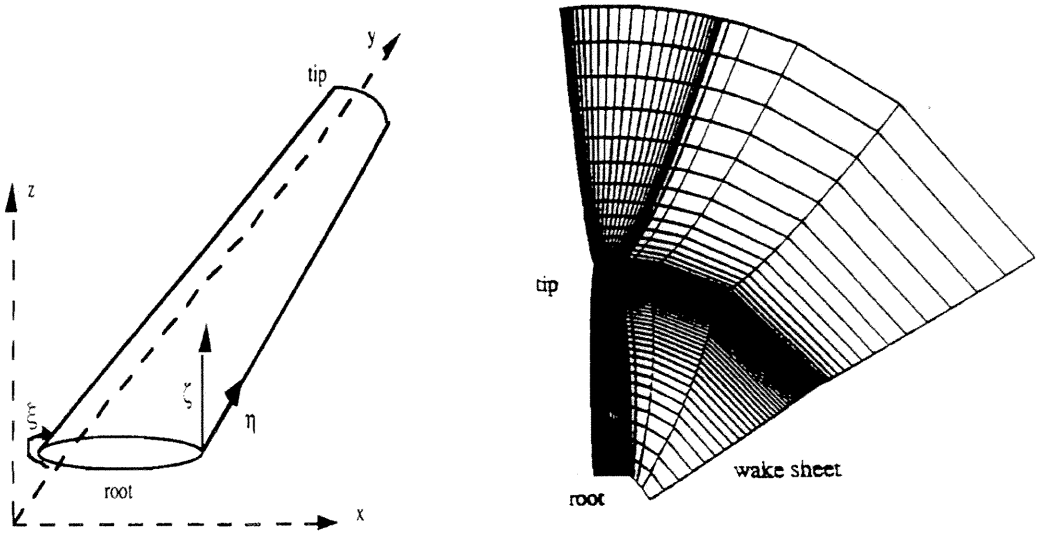

a) coordinate system

b) plan view of grid

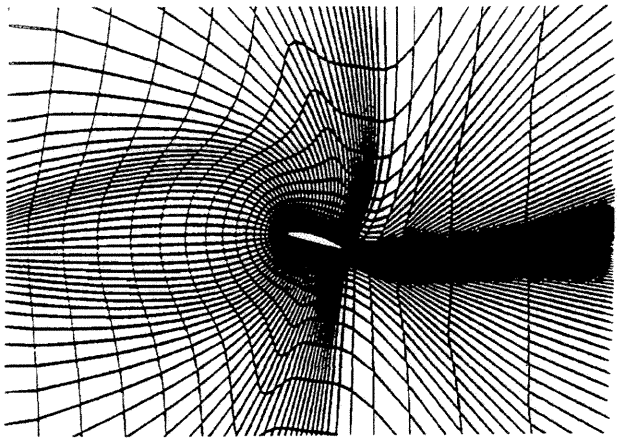

c) grid of blade section at r/R=0.75

Figure 1. Computational grid.

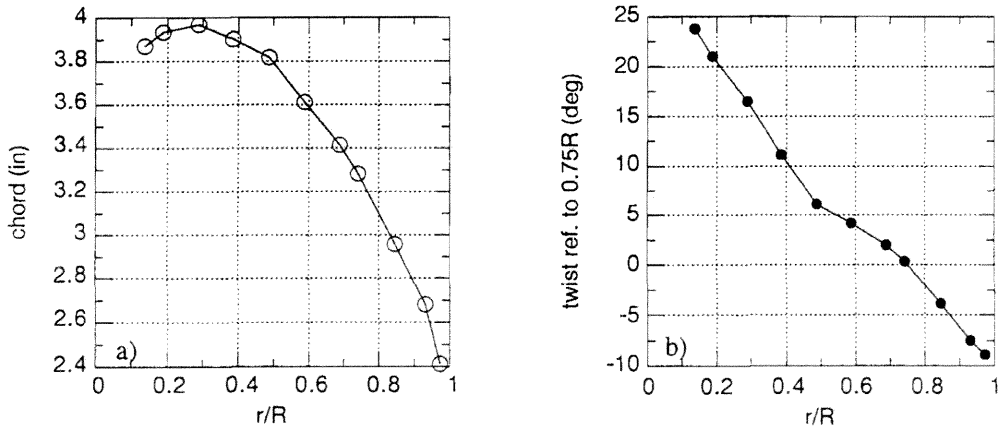

Figure 2. Prop rotor blade properties. a) chord distribution b) twist distribution

Enforcement of the periodic boundary condition caused grid cell skewing, especially when a large collective pitch was imposed; thus, the amount of collective pitch (and subsequently thrust) was limited. Because of the relatively large thickness of the airfoil and the high twist inboard, the root cut-out in the computational domain was extended from 0.11R to 0.198R. Extending the root cut-out avoided generating extremely kinked regions in the grid. Since the root region produces only a fraction of the lift generated by the blade outer region, this approximation was considered acceptable.

Preliminary surface pressure (C_p) calculations revealed premature separation at the trailing edge for low thrust cases. Options to correct this problem included artificially sharpening the trailing edge or decreasing the grid spacing (while maintaining the same number of grid points in the chordwise direction). Since the trailing edge is physically more rounded than sharp, a brief investigation of varying grid spacing at the trailing edge was performed.

6. Effect of Trailing Edge Grid Spacing

Figure 3 shows the effect on C_p of decreasing the grid spacing at the trailing edge while maintaining constant collective pitch and M_{tip}. The total number of grid points defining the airfoil was not changed. Δx_{TAIL}, the parameter which controls the trailing edge spacing, is referenced to the chord at 0.75R. For a collective pitch of 6 deg and M_{tip}=0.33, decreasing Δx_{TAIL} from 0.012 to 0.004 significantly reduces the amount of trailing edge separation which leads to an increase in section thrust, normal force, and torque coefficient, as shown in Figs. 4-6.

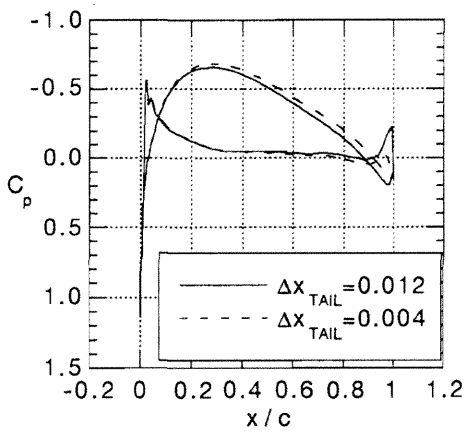

Figure 3. Effect of trailing edge spacing on C_p.

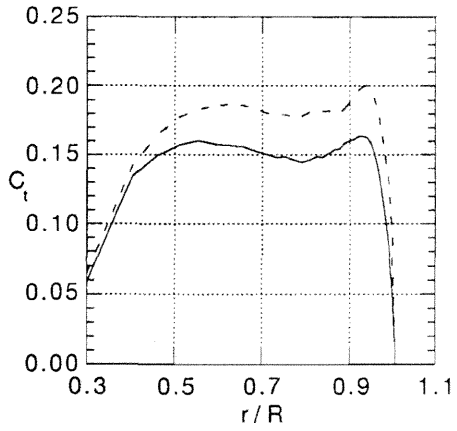

Figure 4. Effect of trailing edge spacing on C_t.

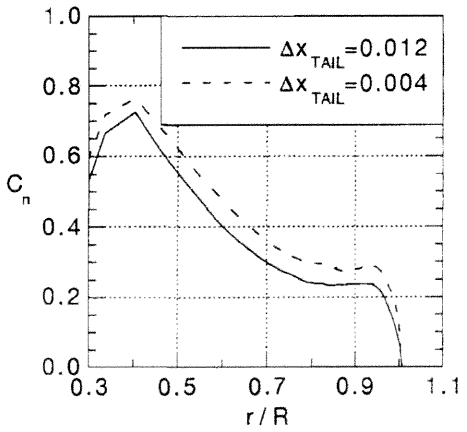

Figure 5. Effect of trailing edge spacing on C_n.

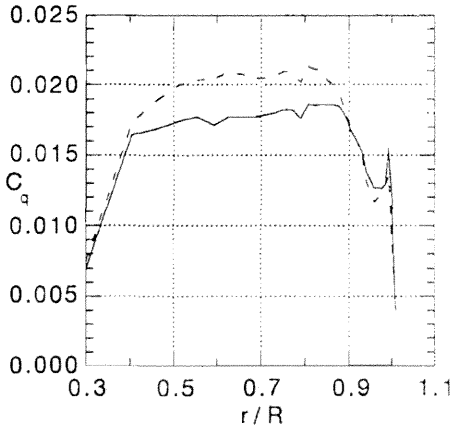

Figure 6. Effect of trailing edge spacing on C_q.

Figures 3 - 6 indicate that if Δx_{TAIL} is made small enough, the loops in the C_p distribution can be reduced to account just for the blunt trailing edge and not any extraneous separation. Practically, this is not possible. As explained earlier, the high twist and the requirement to enforce periodicity at the outer boundaries make the grid generation very sensitive to small changes in grid spacing, especially at large collectives where the volume grid is highly skewed. At the lower collective settings, Δx_{TAIL} values of 0.003 to 0.005 were used; for the higher collective settings (collective $\geq$ 16 deg), a value of approximately 0.012 was the minimum value of Δx_{TAIL} which produced a usable grid (that is, one without negative Jacobians). Note that in subsequent plots, calculated and measured C_T are matched, not collective pitch.

7. Description of experiments

Performance, surface pressures and wake data from a model prop rotor were obtained during two separate experiments using the same rotor. The prop rotor blades were not a scale-model of a particular tilt rotor blade, although the twist distribution (Fig. 2b)) is typical of modern tilt rotor blade. Each three-bladed rotor is made from birch wood and is 4 ft in diameter. Properties of the rotor are shown in Table 1. The experiments are described next.

Table 1. Model Prop Rotor Properties

Number of blades	3
Rotor radius	2 ft
Solidity (Ref. 5)	0.1194
Chord at 0.75 radius	3.3 in
M_{tip} (Ref. 4, 5)	0.19, 0.33, 0.37, 0.45, 0.56, 0.67
Twist	nonlinear

7.1 Shadowgraph experiment

Reference 4 presents shadowgraph data from one prop rotor of a complete, small-scale tilt rotor model. The installation during the experiment consisted of one rotor, one nacelle, and one wing spar (Fig. 7). The experiment was conducted in the settling chamber of the NASA Ames 7- by 10-Foot Wind Tunnel with the rotor plane approximately 2.50 rotor radii above the ground and 0.40 radii above the wing spar. Rotor thrust measurements were made from nacelle-mounted strain gages. The axial and radial tip vortex locations were measured from the shadowgraphs. The wing spar introduced some distortion to the wake geometry; in addition, recirculation effects contributed to the data scatter. Additional details about the experiment are found in Ref. 4.

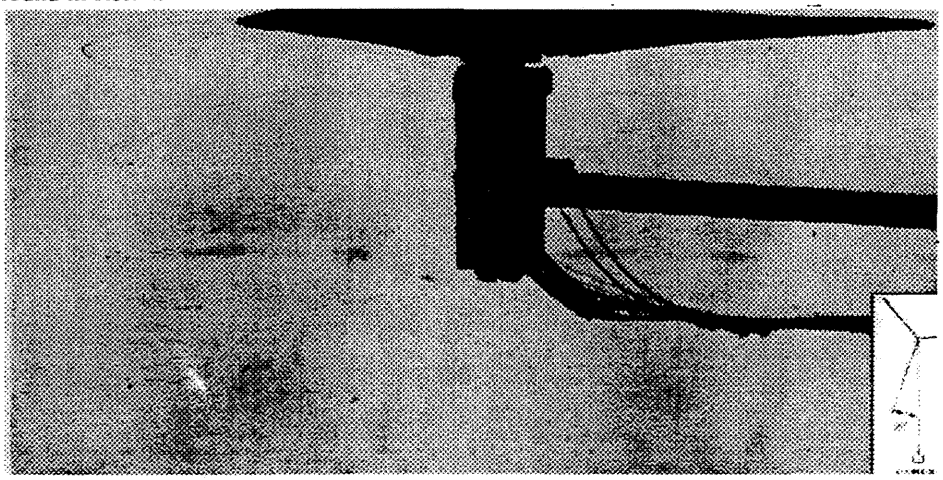

Figure 7. Installation of wing and spar during shadowgraph experiment.

7.2 Hover Chamber Experiment

An isolated, rotor hover experiment using the same rotor of Ref. 4 is described in Ref. 5. The objective of the Ref. 5 experiment was to measure blade surface pressures at high thrust levels. One of the three blades of the rotor system was configured with surface pressure taps. The rotor was installed in the U. S. Army hover chamber at NASA Ames. The rotor plane was approximately 7.5 rotor radii above the chamber floor; the distance from the rotor center to the chamber wall was also 7.5 rotor radii. The chamber was constructed to minimize recirculation effects by allowing the exhaust or wake from the rotor to exit through openings at the side of the chamber floor. Rotor thrust and torque measurements were made using a six-

component strain gage balance. The balance measurement error was estimated to be within a few per cent of the measurement. Additional details of this experiment are found in Ref. 5. The installation set-up of this experiment is shown in Fig. 8.

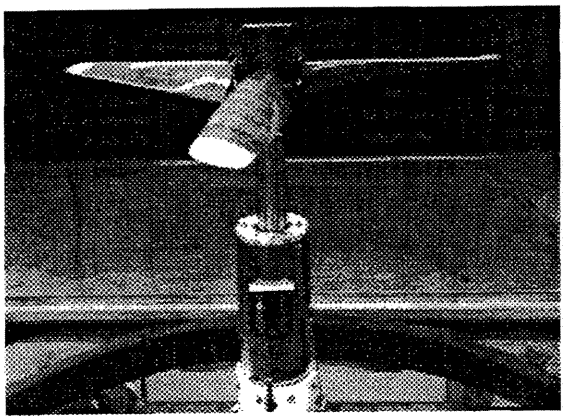

Figure 8. Hover test installation.

8. Results

In the following sections, calculations are compared with data from the hover chamber and shadowgraph experiments. The behavior of the calculated integrated prop loads with solution iteration is presented first. Next, performance, loads and surface pressures are compared with the measurements. Then, calculations of tip vortex location are compared with shadowgraph data.

8.1 Variation of prop rotor loads with solution iteration

Figures 9 and 10 show the effect of solution iteration number on residual and C_T behavior, respectively, for a low and high thrust case at M_{tip}=0.33. The spikes at the 1000 and 4500th iteration are caused by restarting the analysis. Figure 9 shows that the residual for both cases has dropped 3 orders in magnitude and appears on a continued downward trend at 4500 iterations. The integrated thrust coefficient (Fig. 10) has leveled off by the time 4500 iterations has been reached. As a check, the low thrust case was run for another 3500 iterations. Figure 10 shows there is no significant change in C_T at the 8000th iteration compared to the 4500th iteration. In subsequent plots, surface pressures, section loads, and wake geometry results represent the solution at the 4500th iteration. Because of the slight oscillatory behavior of the integrated performance values with iteration number, C_T, C_Q (torque coefficient), and FM (figure of merit) were obtained by computing the average of values from the 3000th to 4500th iteration.

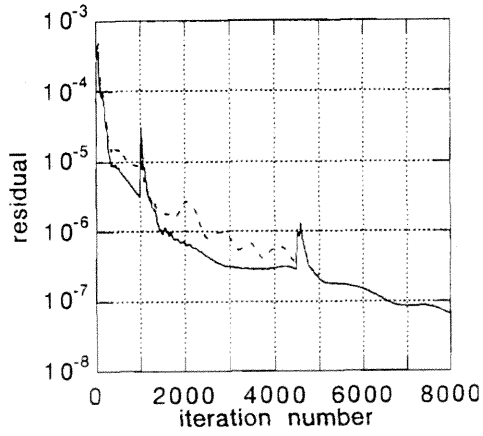

Figure 9. Residual behavior.

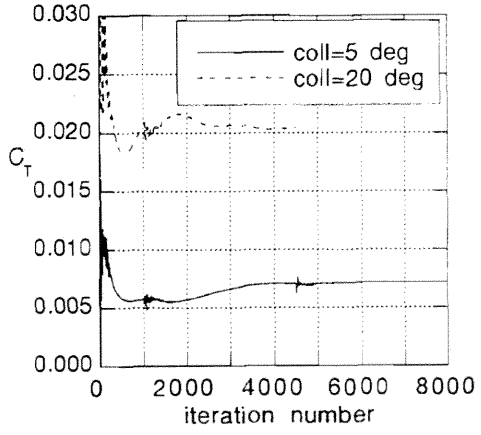

Figure 10. C_T behavior.

8.2 Rotor performance

In order to compare calculated and measured results, the rotor collective pitch was adjusted in the calculations until a satisfactory match with measured rotor thrust coefficient was achieved. This approach was considered more reasonable than simply matching collective pitch, since the settings in either experiment could easily be offset given the method of setting the collective.

Figures 11a) and b) show calculated and measured rotor C_Q and FM as a function of C_T, respectively; for M_{tip}= 0.33. Using the tip Mach number and the chord at 0.75 radial station, the Reynolds number for these cases is 6.53 x10^5. As discussed earlier, the difficulties in decreasing Δx_{TAIL} at the higher collective settings (and hence higher thrust) contribute to the discrepancies between the calculated and measured performance. Differences between calculated and measured FM range from less than 1 per cent at the lower thrust to nearly 7 per cent at the high thrust. The differences at low thrust are on the same order seen in previous investigations to predict hover performance for a helicopter rotor, for example, Refs. 10 and 19.

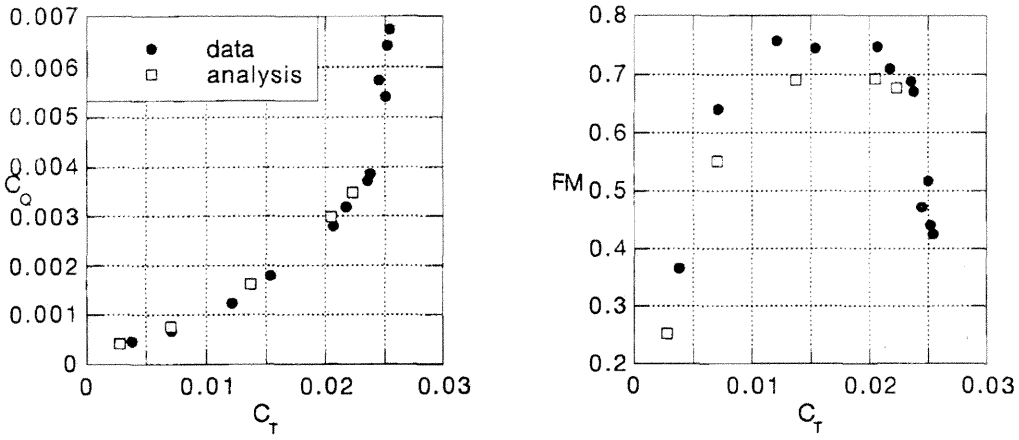

Figure 11. Comparison of prop rotor performance for M_{tip}=0.33. a) C_Q b) FM

8.3 Spanwise Loads

Figure 12 shows the C_n distribution for a low and high thrust case at M_{tip}=0.33. Reference 5 computed C_n, also shown in Fig. 12, from the surface pressure data.

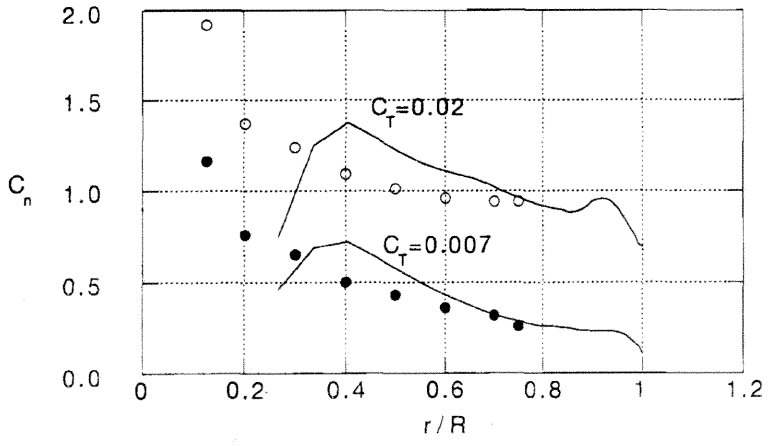

Figure 12. C_n distributions for C_T=0.007 and 0.02; M_{tip}=0.33 (symbols represent C_n values calculated by Ref. 5; solid line represents analysis).

Recall that the analysis models the first spanwise grid station (r/R=0.198) as a solid wall, so comparisons cannot be made at that station (or any station inboard of 0.198). The first spanwise station after the solid wall is located at r/R=0.267. The analysis trend (decreasing C_n) for r/R<0.4 may be influenced by the solid wall boundary condition. The differences between the analysis and the C_n values from Ref. 5 decreases as radial station is increased. The Ref. 5 C_n values should be viewed with caution, however, since there were few pressure measurements near the leading edge.

8.4 Surface pressures

Next, calculated surface pressure coefficients are compared with measured data for the two thrust cases. The local rotational velocity, $0.5\rho_\infty(\Omega r)^2$, was used to compute the pressure coefficients, C_p. Figure 13 shows comparisons for six radial stations for C_T=0.007. Grid stations did not always coincide with stations having experimental data; those stations are indicated in Figs. 13a)-f). Figure 13a shows the data for r/R=0.30; calculations for two radial stations bracketing r/R=0.30 are also shown. Although the shape of the calculated C_p curve is similar to the measured C_p, magnitudes are clearly wrong. There are several contributing factors to this discrepancy. First, although the root boundary condition is improved over the original, the boundary is not a realistic physical representation of the prop rotor hub. Second, the spanwise spacing at the root is coarse, to avoid grid generation problems at large collective pitches. Figures 13 b)-f) show the comparison between experimental and calculated C_p improves with increasing radial station. This is expected since the spanwise spacing becomes finer as the blade tip is approached. The calculations are able to capture the details near the leading edge (see Fig. 13 e) and f)) where the upper and lower C_p distributions cross.

Figure 14 shows similar results for the C_T=0.02 case. Again, the comparison improves as the radial station increases. For r/R=0.50 and greater, the calculations show a large adverse pressure gradient from the leading edge. There is insufficient experimental data to verify the calculated behavior at the leading edge.

Except for the root region, these C_p comparisons have established the ability of the analysis to capture fairly detailed features of the surface pressures near the blade surface. The next section addresses the comparison between measured and computed tip vortex location.

8.5 Wake geometry

Although the surface pressures on the model prop rotor blade compare reasonably well with the experimental data of Ref. 5, an assessment must be made about the ability of the analysis to capture the surrounding flow field. Reference 10 also presented reasonable surface pressure comparisons with measurements, however, calculated flow field vorticity contours revealed the tip vortex located above the blade at the first blade passage.

The shadowgraph data from Ref. 4 will be used to compare measured and calculated tip vortex radial and axial location. The collective pitch during the experiment was 13 deg with M_{tip}=0.56. Because of the uncertainties in the thrust measurements during the shadowgraph experiment (up to 10% error in C_T expected, according to Ref. 4), the thrust corresponding to 13 deg was deduced from a plot of C_T vs. collective pitch measured during the Ref. 5 experiment (for M_{tip}=0.33) which used a rotor balance. The effect of M_{tip} on C_T was assumed small. For a collective of 13 deg, the C_T was found to be 0.017. Calculations were then run to match C_T=0.017.

In order to determine the vortex location from the solution, the vorticity magnitude was first calculated for the entire flow field. Then, azimuthal cuts through the flow field were taken and concentrations of high vorticity were located; the spatial location of the vortex center was then determined. As with the data reduction process of the shadowgraphs, there is some subjectivity involved in determining the vortex location. Figures 15a) and 15b) present measured and calculated axial and radial tip vortex location, respectively. Data from both the right and left sides of the rotor are presented. The presence of the wing spar on the right side of the rotor (Fig. 7) causes the wake to be asymmetrical. Figure 15a) shows the measured descent rate is initially faster than the calculations. The measured contraction rate is also initially faster than the calculated rate (Fig. 15b)). The calculations at higher wake age more closely match the measurements taken on the left side of the rotor than the right side. This is reasonable since the presence of the spar is not accounted for in the analysis. As the wake age increases, determining the vortex location from the calculated flow field becomes increasingly difficult because the vorticity becomes more diffuse. This results in small excursions from a smooth trend in the analysis, as shown in Fig. 15b) for wake ages of 270-300 degrees. The correlation presented in Figs. 15a) and 15b) shows the analysis is able to reasonably capture the flow field features. The differences in measured and calculated tip vortex location may be caused by using the incorrect C_T value (0.017) as a target for the analysis. Other factors contributing to the differences include grid resolution in the wake and artificial vorticity dissipation of the flow solver.

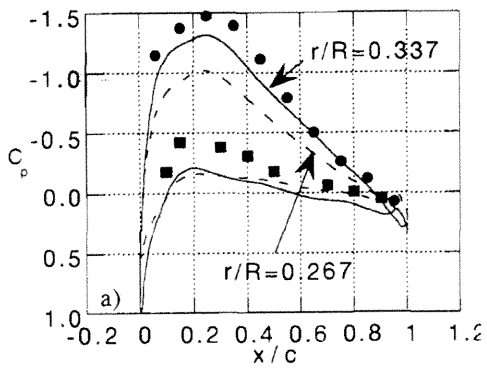

a) r/R=0.30

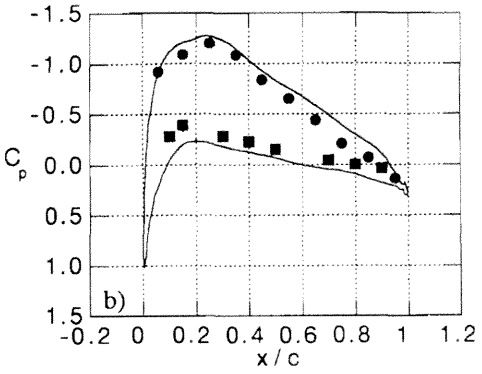

b) r/R=0.40

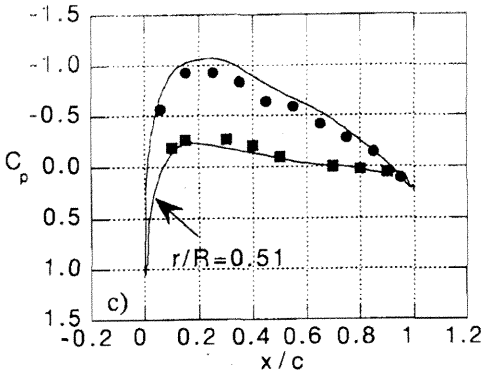

c) r/R=0.50

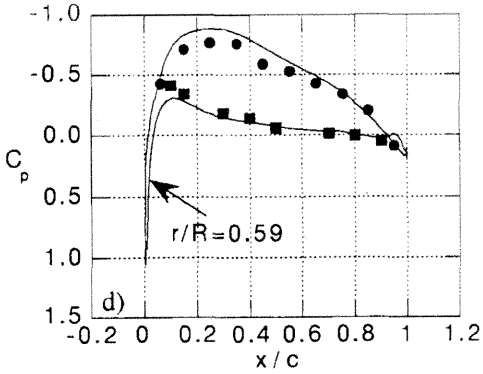

d) r/R=0.60

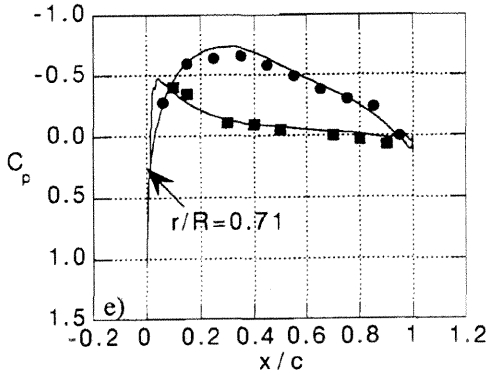

e) r/R=0.70

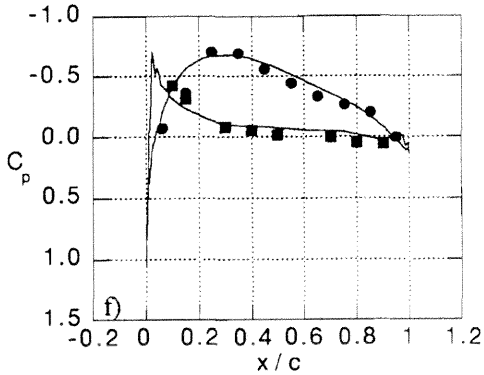

f) r/R=0.75

Figure 13. C_p distributions for C_T=0.007 and M_{tip}=0.33 (data - solid symbols; analysis - curve).

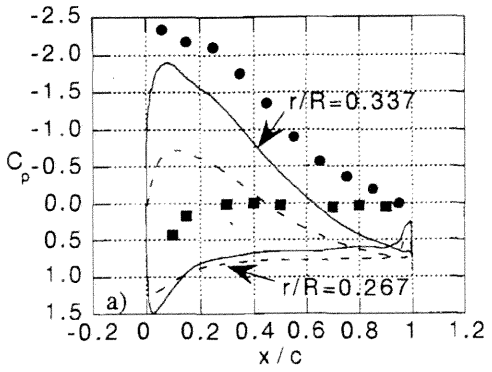

a) r/R=0.30

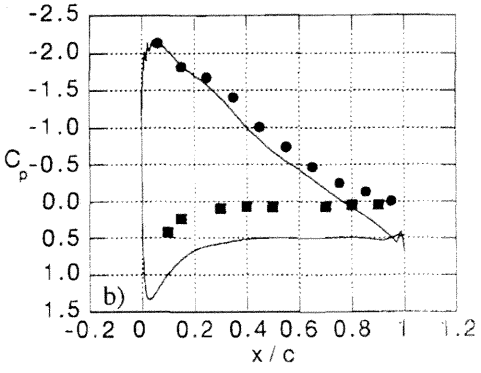

b) r/R=0.40

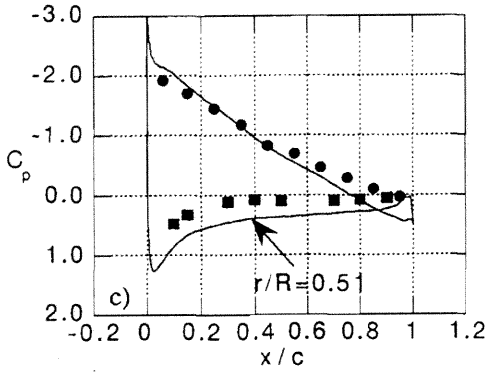

c) r/R=0.50

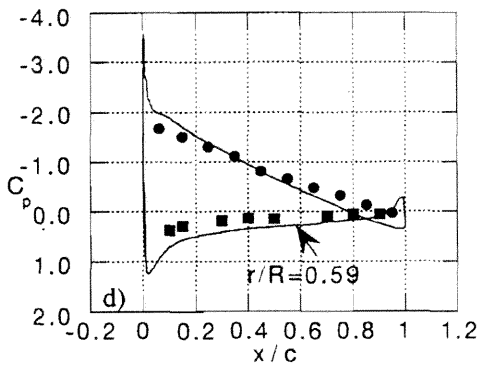

d) r/R=0.60

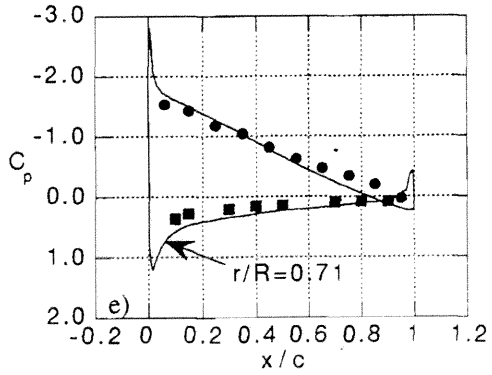

e) r/R=0.70

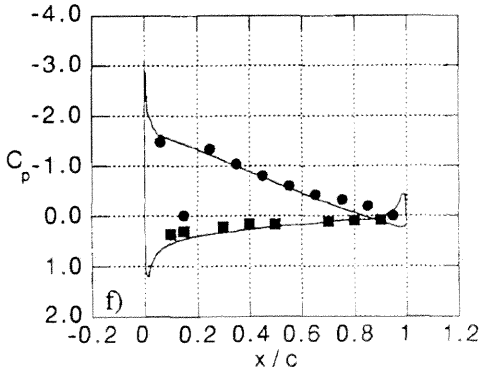

f) r/R=0.75

Figure 14. C_p distributions for C_T=0.02 and M_{tip}=0.33 (data - solid symbols; analysis - curve).

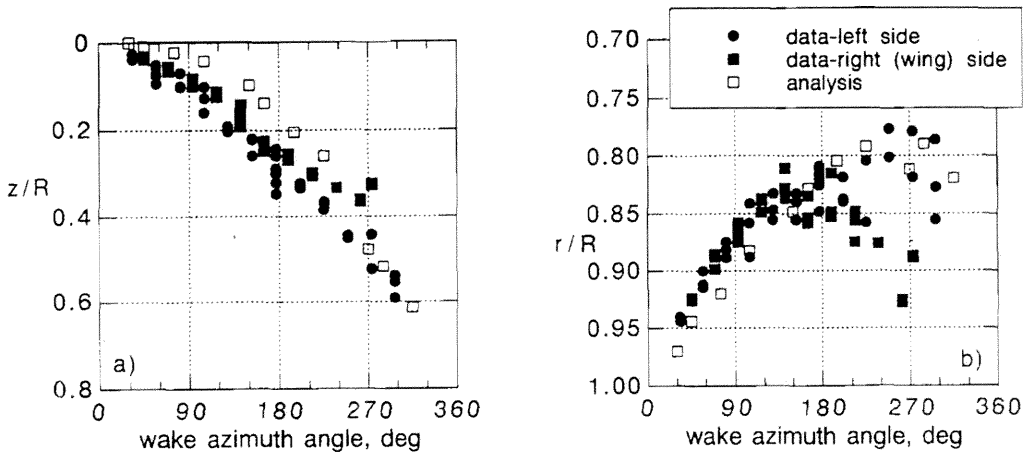

Figure 15. Wake geometry comparison; C_T=0.017 and M_{tip}=0.56. a) descent rate b) contraction rate

9. Conclusions

The flow field of a highly-twisted model prop rotor was analyzed using a thin-layer Navier-Stokes analysis. Modifications to the blade root and far-field boundary conditions in the analysis were investigated. Calculations were compared with measured hover performance, blade surface pressure data, and wake geometry. Specific findings from the investigation are discussed below.

Limitations of the single-block grid generator were encountered near the blade root when modeling the highly-twisted prop rotor blade. Enforcement of the periodic boundary condition caused grid cell skewing, especially when a large collective pitch was imposed; thus, the amount of collective pitch (and subsequently thrust) was limited. The exercise in varying trailing edge spacing, however, did establish that thrust calculations can be improved if finer spacing is used.

Differences in calculated and measured figure of merit ranged from less than one per cent at very low thrust to nearly 7 per cent at high thrust. Comparisons between calculated C_n and C_n values from Ref. 5 improved with increasing radial station. For both low and high thrust cases, correlation with surface pressures improved with increasing radial station. Tip vortex descent rate and contraction rate were initially less than the measured rates.

10. Recommendations

During the course of this investigation, a number of topics deserving a more thorough treatment were encountered. These areas are discussed below.

The grid generator and the enforcement of the periodic boundary condition caused several limitations to this study. First, grids generated for large blade twist distributions with a large collective pitch imposed were very sensitive to grid spacing parameters and grid density, preventing a more comprehensive investigation of grid effects on the solution. Second, a usable grid could not be generated using the true root cut-out of the model prop rotor, so the cut-out was extended. These limitations can possibly be overcome if overset grids are used instead of a single-block grid. The periodic boundary condition might still be a problem, however, since the grid at the upstream and downstream planes will still require matching. Modeling all three blades using overset grids and running an unsteady analysis will eliminate the need for the periodic boundary condition, but the computational cost will increase dramatically. Perhaps using overset grids with unstructured grids away from the blade surface and still enforcing the periodic boundary condition may be a worthwhile compromise. The root boundary condition can be further improved by using overset grids to model the hub correctly. Further investigation of the far-field boundary condition is required. Implementing higher-order differencing schemes and higher-order metric evaluation may hold promise for preventing diffusion of the vorticity in the wake.

Finally, there is a paucity of airloads and wake measurements for highly twisted rotors and no visualization measurements which reveal the flow behavior on the blade surface. Flow visualization of the blade surface (e.g. oil) is crucial in determining if calculations are accurately predicting the onset and growth of stalled regions.

11. Acknowledgements

The authors thank Dr. Chee Tung, U.S. Army Aeroflightdynamics Directorate, and Mr. Thomas Norman, NASA Ames, for the data from the model prop rotor experiments. The assistance of Mr. Peter Talbot and Mr. Willie Wallace, Jr. in obtaining the coordinates of the prop rotor blade is gratefully acknowledged.

12. References

1. F.F. Felker, M.D.Betzina, and D.B. Signor. Performance and Loads Data from a Hover Test of a Full-Scale XV-15 Rotor. NASA TM 86833, November 1985.

2. F.F. Felker, D.B. Signor, L.A. Young, and M.D. Betzina. Performance and Loads Data from a Hover Test of a Full-Scale Advanced Technology XV-15 Rotor. NASA TM 86854, April 1986.

3. F.F. Felker, L.A. Young, and D.B. Signor. Performance and Loads Data from a Hover Test of 0.658 Scale V-22 Rotor and Wing. NASA TM 89419, April 1987.

4. T.R. Norman and J.L. Light. Rotor Tip Vortex Geometry Measurements Using the Wide-Field Shadowgraph Technique. *Journal of the American Helicopter Society*, Vol. 32, (2), April 1987.

5. C. Tung and L. Branum. Model Tilt-Rotor Hover Performance and Surface Pressure Measurement. 46th Annual National Forum of the American Helicopter Society, Washington, D.C., May 1990.

6. J.C. Narramore and R. Vermeland. Navier-Stokes Calculations of Inboard Stall Delay Due to Rotation. *Journal of Aricraft*. Vol. 29, (1), January-February 1992.

7. G.K. Yamauchi and W. Johnson. Navier-Stokes Calculations for a Highly-Twisted Rotor Near Stall. American Helicopter Society Aeromechanics Specialists Conference, San Francisco, CA, January 1994.

8. Meakin, R. Unsteady Simulation of the Viscous Flow About a V-22 Rotor and Wing in Hover. AIAA Atmospheric Flight Mechanics Conference, AIAA Paper No. 96-3463, Baltimore, MD, August 1995.

9. G.R. Srinivasan, J.D. Baeder, S. Obayashi, and W.J. McCroskey. Flowfield of a Lifting Hovering Rotor - A Navier-Stokes Simulation. Sixteenth European Rotorcraft Forum, Glasgow, Scotland, September 1990.

10. B.E. Wake and J.D. Baeder. Evaluation of the TURNS Analysis for Hover Performance Prediction. American Helicopter Society Aeromechanics Specialists Conference, San Francisco, CA, January 1994.

11. C. Tung and S. Lee. Evaluation of Hover Performance Prediction Codes. 50th Annual National Forum of the American Helicopter Society, Washington, D.C., May 1994.

12. T.H. Pulliam and J.L. Steger. Implicit Finite-Difference Simulations of Three-Dimensional Compressible Flow. *AIAA Journal*, Vol.18, (2), February 1980.

13. G.R. Srinivasan, G.R., W.J. McCroskey, J.D. Baeder, and T.A. Edwards. Numerical Simulation of Tip Vortices of Wings in Subsonic and Transonic Flows. AIAA/ASME 4th Fluid Mechanics, Plasma Dynamics and Lasers Conference, AIAA Paper No.86-1095, Atlanta, GA, May 1986.

14. G.R. Srinivasan and W.J. McCroskey. Navier-Stokes Simulations of Tip Vortices for Fixed and Rotating Helicopter Blades. International Symposium on Computational Fluid Dynamics, Sydney, Australia, August 1987.

15. G.R. Srinivasan and W.J. McCroskey. Navier-Stokes Calculations of Hovering Rotor Flow Fields. *Journal of Aircraft*, Vol.25, No.10, October 1988. (AIAA Atmospheric Flight Mechanics Conference, Monterey, CA, AIAA Paper No.87-2629-CP, August 1987).

16. S. Obayashi. Numerical Simulation of Underexpanded Plumes Using Upwind Algorithms. AIAA Atmospheric Flight Mechanics Conference, AIAA Paper No.88-4360-CP, Minneapolis, MN, August 1988.

17. G. Yamauchi. Flow Field Analysis of Highly-Twisted Rotors in Hover. PhD Thesis (to be published), Stanford University.

18. K. Fujii and S. Obayashi. Navier-Stokes Simulations of Transonic Flows over a Wing-Fuslage Combination. *AIAA Journal*, Vol. 25, (12), December 1987.

19. G.R. Srinivasan, V. Raghavan,and E-P.N. Duque. Flowfield Analysis of Modern Helicopter Rotors in Hover by Navier-Stokes Method. International Technical Specialists Meeting, Rotorcraft Acoustics and Rotor Fluid Dynamics, Philadelphia, PA, October 1991.

20. D.A. Saunders, R.A. Kennelly, Jr., and L.C. Kennelley. Aerodynamics Division Software Library. NASA Reference Publication 1276, June 1992.